

TRACKING THE DISTRIBUTION OF ²⁶Al AND ⁶⁰Fe DURING THE EARLY PHASES OF STAR AND DISK EVOLUTION

MICHAEL KUFFMEIER

<University of Copenhagen>

TROELS FROSTHOLM MOGENSEN

<University of Copenhagen>

TROELS HAUGBØLLE

<University of Copenhagen>

MARTIN BIZZARRO

<University of Copenhagen>

ÅKE NORDLUND

<University of Copenhagen>

Abstract

The depleted abundance of ²⁶Al in Calcium Aluminum rich Inclusions (CAIs) with Fractionation and Unidentified Nuclear isotope effects (FUN) compared to bulk CV CAIs by factors of more than 10 has led to the idea that ²⁶Al enhanced gas has been injected into the Early Solar System by a Supernovae injection within the early phase of the formation of the Sun. In this paper, we present for the first time results for the evolution of nine stars properly embedded in the surrounding giant molecular cloud obtained by zoom-simulations carried out with the adaptive-mesh refinement code RAMSES by solving the equations of ideal magnetohydrodynamics. We find ²⁶Al/²⁷Al as well as ⁶⁰Fe/⁵⁶Fe ratios within a vicinity of about 1000 AU of the stars that closely follow the predicted decay curve of the initial abundance at time of star formation without any signs of neither spatial nor temporal heterogeneities for the first more than 100 ka of star formation. Hence, the observed differences in ²⁶Al/²⁷Al ratios between FUN and canonical CAIs are most likely not caused by supernovae injections in the early phase of star formation. However, we find possible differences in short-lived radionuclides abundances for times later than 100 ka. Order of magnitude estimates of the possibility for protoplanetary disk pollution by CAIs originally formed in other solar systems indicate such a scenario as unlikely. Thus, we propose thermal processing of dust grains - not included in our models - as a probable explanation for the observed heterogeneities in ²⁶Al/²⁷Al ratios.

<Journal approved keywords>

1. INTRODUCTION

Giant molecular clouds (GMCs) are the primary reservoirs of cold, star-forming gas in the Galaxy. Astronomical observations and numerical simulations of star-forming regions suggest that GMCs have typical lifetimes of a few tens of Ma (Padoan et al. 2015; Dobbs et al. 2014; Kawamura et al. 2009; Fukui et al. 1999; Bash et al. 1977; Blitz & Shu 1980), during which multiple episodes of star formation may take place. Stars more massive than eight solar masses eventually end their lives in type II supernova explosions and, during these events, pollute their environments with nucleosynthetic products. As such, the nucleosynthetic make-up of a protostellar core is expected to reflect a mixture of an old galactically-inherited component with younger supernova-derived material, including freshly-synthesized radioactive ²⁶Al and ⁶⁰Fe, produced during the lifetime of the GMC. The γ -ray emis-

sions from the radioactive ²⁶Al and ⁶⁰Fe nuclei, observable throughout the Milky Way due to the low opacity of γ -rays, have been used to determine the steady-state ISM abundance of ²⁶Al and ⁶⁰Fe and, hence, an estimate of the Galactic ⁶⁰Fe/²⁶Al ratio (Diehl et al. 2006; Wang et al. 2007).

Meteorites and their components provide insights into the formation history of the earliest solar system, including the birthplace of the Sun. The most primitive meteorites, chondrites, contain calcium-aluminum-rich inclusions (CAIs) representing the oldest dated solar system solids, formed 4567.30 ± 0.16 Ma ago (Connelly et al. 2012). These sub-millimeter-to-centimeter objects are thought to have formed as fine-grained condensates from a gas of approximately solar composition, in a region with high ambient temperature ($>1,300$ K) and low total pressures (10^{-4} bar) (Tielens & Al-lamandola 1987; Ebel & Grossman 2000), possibly during a brief ($<10,000$ years) (Larsen et al. 2011) heating event temporally associated with the very earliest phase of the proto-sun (Krot et al. 2009). The presence in CAIs of the short-lived radioisotope ¹⁰Be formed by solar energetic particle irradiation (McKeegan et al. 2000) is further evidence that they formed in

<kueffmeier@nbi.dk>

¹ Visiting Astronomer, etc.² Current Address, etc.³ Visiting Astronomer, etc.

the vicinity of the protosun. Importantly, CAIs typically contain evidence for an early presence of ^{26}Al , defining a canonical initial $^{26}\text{Al}/^{27}\text{Al}$ ratio of 5×10^{-5} (MacPherson et al. 1995; Jacobsen et al. 2008; Larsen et al. 2011). This initial abundance is approximately 10 times higher than that expected from the galactic background abundance, apparently requiring a late-stage seeding of the protosolar molecular cloud core from a nearby supernova. However, numerical simulations of the production, transport, and admixing of freshly synthesized ^{26}Al in star-forming regions within giant molecular clouds (Vasileiadis et al. 2013) indicate that, under typical star formation conditions, the levels of ^{26}Al in most star-forming regions are comparable to that deduced from CAIs. Thus, the presence of short-lived radionuclides such as ^{26}Al in the early solar system does not require special circumstance but rather represent a generic feature of the chemical evolution of giant molecular clouds.

However, a class of refractory grains and inclusions believed to be temporally related to the formation of canonical CAIs record much lower levels of ^{26}Al corresponding to initial $^{26}\text{Al}/^{27}\text{Al}$ of $< 5 \times 10^{-6}$ (Fahey et al. 1987). Of interest are the coarse-grained refractory inclusions with fractionation and unidentified nuclear effects (FUN CAIs, (Wasserburg et al. 1977)), which, in addition to their low initial abundance of ^{26}Al , are characterized by large mass-dependent fractionation effects and nucleosynthetic anomalies in several elements. Moreover, the abundance of rare earth elements and the oxygen isotope composition of FUN CAIs indicate that their precursors formed as condensates from a solar gas (Holst et al. 2013). Collectively, these observations are often interpreted as reflecting formation of FUN CAIs prior to the admixing of stellar-derived ^{26}Al to the CAI forming gas (Sahijpal & Goswami 1998; Thrane et al. 2008; Makide et al. 2011; Pan et al. 2012). If this interpretation is correct, these objects can be used to track the timing of addition of ^{26}Al to the forming protoplanetary disk. Alternatively, the contrasting initial ^{26}Al abundance of canonical and FUN CAIs may reflect unmixing of two distinct dust components by thermal processing (Trinquier et al. 2009; Paton et al. 2013; Schiller et al. 2015), namely an old, galactically-inherited homogeneous dust from a new, supernovae-derived dust component formed shortly prior to or during the evolution of the giant molecular cloud to the protosolar molecular cloud core. Such a bi-modal dust distribution can either be achieved by having separate populations of grains, or having old grains being covered with newly synthesised gas condensates, resulting in a multilayered grain-structure. Distinguishing between these two interpretations is critical for understanding the origin and distribution of short-lived radionuclides in the early solar system.

In this paper, we use GMC-scale adaptive mesh-refinement numerical simulations to trace the abundance of ^{26}Al and ^{60}Fe in star-forming gas during the early stages of accretion of individual low mass protostars. We first model the star formation process on the time scale of an evolving GMC structure, and use additional adaptive mesh refinement to zoom in on individual stars, allowing us to study the accretion dynamics of individual stars and their disks down to scales of a few astronomical units. This approach allows us, for the first time, to evaluate the level of ^{26}Al and ^{60}Fe heterogeneity during the early evolutionary stages of individual protostars that may result from the variable contributions of different supernova

sources during the lifetime of the GMC structure.

More than 200 stars with masses of at least $0.2 M_{\odot}$ form during our simulation, of which we select ten stars that end up having about 1-2 solar masses and one of about 7 solar masses for detailed high-resolution zoom-in investigations. Our models indicate a homogeneous level of ^{26}Al in the accreting gas for all systems during the first 100 ka of their formation, although some level of heterogeneity is possible in the later evolutionary stages. Therefore, the contrasting initial $^{26}\text{Al}/^{27}\text{Al}$ ratios recorded by canonical and FUN CAIs cannot easily be reconciled heterogeneous accretion processes.

2. METHODS

The simulations were carried out with the magnetohydrodynamic (MHD) adaptive mesh refinement (AMR) code `RAMSES` (Teyssier 2002; Fromang et al. 2006). We solve the equations of ideal magnetohydrodynamics using an MUSCL Godunov method with a constrained transport HLLD solver (Miyoshi & Kusano 2005) using a multiple dimensional MonCen slope limiter. To maintain numerical stability in super-sonic flows, and ensure a reasonable time-step, cells where the combined advection and fast-mode speed – the total signal velocity – is above about 150 km s^{-1} are evolved with a more diffusive local Lax-Friedrichs solver. In `RAMSES` the adaptive mesh is described with a fully threaded oct-tree, and a cell refined to level $n + 1$ has half the size compared to a cell refined to level n . Refinement can be done according to a variety of criteria. The basic criterium used in this paper is a Truelove density-based refinement with a factor of 4 increase in threshold density for each level of refinement, resulting in a constant minimum number of cells per Jeans-length (Truelove et al. 1997). This is complemented with a number of refinement criteria based on gradients in density, pressure, and magnetic fields, as described below.

To model a star forming region, we include self-gravity, cooling parameterized with a table lookup based on Gnedin & Hollon (2012), heating from cosmic rays, and photoionization Osterbrock & Ferland (2006) with a density dependent exponentially cut-off of 500 cm^{-3} (Franco & Cox (1986). For a more detailed description of the thermodynamics see also Padoan et al. (2015). When the gas reaches a density where a Jeans length at the highest level of refinement is resolved with only a few cells, and several other criteria are fulfilled (see below), sink particles are inserted that interact with the gas through accretion (Padoan et al. 2012, 2014, cf.). Sink particles more massive than $8 M_{\odot}$ eventually explode as supernovae, with a delay time (stellar life time) given by a mass-dependent lookup table (Schaller et al. 1992). Fresh SLR material is injected into the SN ejecta according to the mass-dependent yields given in (Limongi & Chieffi 2006).

2.1. Setup and initial evolution for a GMC

The current simulation is a partial rerun, with much higher numerical fidelity, of the model in Vasileiadis et al. (2013), which uses a $(40 \text{ pc})^3$ periodic box with a total mass of a total mass of $9 \times 10^4 M_{\odot}$, and a mean magnetic field of $3.5 \mu\text{G}$. That model was started up by driving turbulence with a typical root mean square velocity of 6-7 km/s (Padoan & Nordlund 2011), consistent with Larson’s velocity dispersion-size relation $\sigma(\text{km s}^{-1}) \propto L_{\text{pc}}^{0.38}$ (Larson 1969, 1981). Self-gravity was then turned on, and subsequently, sufficiently dense gas was converted to a distributions of sink particles, sampled according to a Salpeter initial mass function (IMF) (Padoan

& Nordlund 2002). When the kinetic energy feedback due to supernovae explosions became significant, the turbulence driving was turned off, and the evolution was continued with the RAMSES code, with a root grid of 128^3 and 16 levels of refinement relative to the box size; i.e. with a minimum cell size of about 126 AU. Essentially the same star formation recipe as described below was used to selfconsistently follow the formation of massive stars, which gradually took over driving from the generation of massive stars originating from IMF sampling. The result was a realistic, evolving giant molecular cloud model, polluted through SNe explosions with SLRs, and having a mature and diverse population of massive stars (cf. Vasileiadis et al. 2013, for details). Here we repeat part of this run, with an updated version of RAMSESthat provides higher fidelity than the version used by Vasileiadis et al. (2013), by allowing more aggressive choices of Riemann solver and slope limiter. Snapshots from this simulation were selected as starting points for the current zoom simulations. In the current paper we define $t=0$ as the time of birth of the first massive star formed in the Vasileiadis et al. (2013) RAMSESRUN.

2.2. Sink particle creation and accretion

The stars are mimicked by sink particles that form when cold gas on the highest refinement level exceeds a certain threshold density, has a convergent velocity flow, is at a local minimum of the potential, and is at least 30 cells (≈ 3777 AU) from any already formed sink particle. Over time, it is evident that stars form clustered in filaments of high density in contradiction to the classical model of stars forming isolated due to gravitational collapse (Shu 1977). This is consistent with results obtained by numerical simulations of other groups (e.g. Hennebelle (2013); Myers et al. (2014), Banerjee & Körtgen (2015)) and as seen in observations (Lada & Lada 2003; Bressert et al. 2010). This demonstrates the necessity of our more complex large-scale zoom-in model, instead of idealized spherical core collapse models. The sink particles move through the molecular cloud, accreting gas from surrounding cells within a radius of 8 cells from the sink if the gas total energy is negative. The rate of accretion increases gradually from zero at the edge to fraction ≈ 0.01 per orbital time near the sink particle, similar to the prescription given in (Padoan et al. 2014).

Galilean transformations of the rest frame make it possible to turn on the built-in RAMSESgeometric refinement and keep the particle centered, allowing us to explicitly zoom to the environment around the sinks of interest. The geometric refinement in RAMSESDoes not force refinement, but allows one to gradually increase the level of refinement that explicit refinement criteria can trigger. Here we allow refinement in concentric spherical regions with radii of 40 cells at each refined level.

Self-gravity in the simulation is accounted for in three steps: first, we compute the potential from only the gas, using it to compute the gravitational force from the gas on the sink particles. Second, we deposit the sink particle masses to the grid using a triangular shaped cloud (TSC) method and use the combined potential from the gas and sink particles to compute the gravitational forces on the gas. Finally, the gravitational forces between sink particles are accounted for by explicitly using Newtons law, and particles are evolved with a symplectic kick-drift-kick integrator (Springel 2005). This ensures that close encounters between particles are properly accounted for.

2.3. Zoom-in on individual stars

To follow the formation of single stars in detail, while simultaneously retaining realistic initial and boundary conditions of the surrounding medium in the model, we use the method of zoom-in first introduced in Nordlund et al. (2014). A snapshot just before the star is formed is selected, and the gas is allowed to collapse gravitationally, but this time using up to 13 to 15 AMR levels, instead of 9 levels, in close vicinity of the pre-stellar core. This corresponds to a minimum cell size between 8 AU and 2 AU. Our simulations of star formation thus resolve the processes during individual star formation without neglecting the large-scale dynamical effects that govern the motions in the GMC.

In agreement with the natural hierarchy of star formation in space and time, we model the process of star formation and early disk formation in two steps. First, we simulate the evolution of the entire box for approximately 5 Ma with a maximum resolution of 126 AU. During this step, several hundred stars of different masses are formed from which eleven stars are selected. Ten of these stars accrete to 1 to $2 M_{\odot}$ and for comparison reasons, we choose one that accretes about $7.5 M_{\odot}$ (see table 1). In the second step, we rerun the simulation with higher resolution around the selected stars to follow the accretion onto these individual stars in more detail. Our choice of selecting stars that accrete to more than $1 M_{\odot}$ is motivated by the fact that young stars eject a fraction of the accreting mass in strong outflows, which we do not resolve with a resolution of 126 AU, but (partly) resolve when zooming in. Consequently, in order to model the formation and evolution of what becomes solar mass stars, we need to select stars that accrete more than $1 M_{\odot}$ in the broad low resolution run.

The maximum resolution used for the zoom simulations around the selected sinks is either 2 or 8 AU and their evolution is simulated for about 100 ka with a cadence of output files between 200 to 1000 years. Times of formation for the selected sinks in the parental run are 631.300 ka, 667.330 ka, 1742.670 ka, 2054.717 ka, 2212.038 ka, 2470.775 ka, 2576.202 ka, 2653.035 ka, 3156.576 ka, 3270.929 ka and 3389.311 ka.

To ensure proper resolution of the early phase of star formation, we started most zoom simulations several ten thousand years before formation of the selected star. Simultaneously, we also insert about 10 million tracer particles in a cubic region of about 1.28×10^5 in diameter for the zoom-in runs (except for three). The tracer particles are distributed with a probability density proportional to mass density, and are passively advected with the gas motion. In table 1, we provide an overview of the different refinement settings for the selected sinks. The selected stars are formed at different points in time and different environments, from collapsing pre-stellar cores located in filamentary structures of the GMC.

3. DISTRIBUTION OF SLRS IN SPACE AND TIME ON DIFFERENT SCALES

In this Section, we present the distribution of ^{26}Al and ^{60}Fe abundance in a Giant Molecular Cloud, as obtained in our simulations. We present and discuss the evolution and distribution of the SLRs in the entire GMC of $(40 \text{ pc})^3$ according to our AMR simulation with a maximum resolution of 126 AU, which corresponds to a maximum level of refinement of 16 orders of magnitude 2 (i.e. $\frac{40 \text{ pc}}{2^{16}} = 126 \text{ AU}$). In the following, we refer to this run as our parental run. First, we analyze the distribution of the SLRs in the gas phase of the entire GMC

Nr of star	Max. resolution in AU	Formation in parental run in ka	x-coord. in pc	y-coord. in pc	z-coord. in pc
1	2	631.300	33.1767	30.8145	7.8201
2	2	667.330	13.4881	27.3978	25.5582
3	2	1742.670	11.1347	10.9181	0.0509
4	2	2054.717	11.9002	9.4830	27.4879
5	8	2212.038	37.8777	27.3114	32.9574
6	2	2470.775	3.2214	9.2446	3.2398
7	2	2576.202	3.5445	8.9384	2.6478
8	2	2653.035	10.1717	12.3155	3.3944
9	2	3156.576	9.3055	11.9879	32.3207
10	8	3270.929	26.0705	29.2790	2.5924
11	2	3389.311	3.3072	4.6017	2.2056

Table 1
Overview of the eleven stars selected for zoom-in.

and discuss how it affects the abundance in and around the stars. Afterwards, we elaborate in more detail on the SLR abundance around particular stars, by zooming in with a maximum resolution of 2 AU (22 levels of refinement) on nine stars, and with a maximum resolution of 8 AU (20 levels of refinement) around 2 stars. We distinguish between the early (first ~ 100 ka after star formation) and late phase (times later than ~ 100 ka).

3.1. Distribution of SLRs in the gas phase of the GMC

During the roughly 4 Ma of GMC evolution considered for this paper, nine of the massive stars adopted from the previous STAGGER and RAMSES runs explode as supernovae after their mass dependent life times and inject ^{26}Al as well as ^{60}Fe at different locations in the GMC.

In Fig. 1, we show the average mass-weighted abundance of ^{26}Al (left panel) and ^{60}Fe (right panel) as green horizontal lines together with the abundances of the individual stars of masses from 0.2 to $0.5 M_{\odot}$ (purple asterisks), 0.5 to $2.5 M_{\odot}$ (black asterisks) and 2.5 to $8 M_{\odot}$ (yellow asterisks) at their times of formation. The initial abundance of ^{26}Al and ^{60}Fe in the cloud prior to the first supernovae explosion reflect contributions from earlier SN events that occurred prior to our $t=0$. It is clear from Fig. 1 that the average ^{26}Al and ^{60}Fe abundances in the cloud are highly modulated by SN events (illustrated by the blue stars on top of the plots), followed by a gradual decrease due to radioactive decay. The first supernovae corresponds to a star of $13.4 M_{\odot}$ and result in a significant enhancement of the ^{26}Al abundance relative to ^{60}Fe . There are two reasons for this. First, ^{26}Al decays about three times faster than ^{60}Fe and, hence, the ^{60}Fe abundance is depleted less than ^{26}Al before the first SN event. Second, the first SN event is not a very massive star, which produces less ^{60}Fe per unit mass relative to more massive supernovae. The second supernova explodes with a mass of $22.2 M_{\odot}$ less than 200 ka later and significantly enriches the cloud in ^{60}Fe as it is more efficient in producing ^{60}Fe than the first SN. During the time until the next SN explosion, one can clearly recognize the characteristic decay of both SLRs before the box gets efficiently enriched in SLRs by the third SN. This SN is the most massive one during the entire evolution of the GMC with

$75.0 M_{\odot}$ and is thus particularly responsible for the enhancement in ^{60}Fe . The subsequent SNe, with masses $15.3 M_{\odot}$, $29.2 M_{\odot}$, $39.6 M_{\odot}$, $13.2 M_{\odot}$, $22.4 M_{\odot}$ and $29.2 M_{\odot}$ do not enhance the average abundance as much, partly because enrichments of the already enhanced GMC appear less significant on the logarithmic scale. In general, we can see an overall increase of SLR abundances (ranging from about 2.5×10^{-6} to about 1×10^{-4} for $^{26}\text{Al}/^{27}\text{Al}$ and from about 5×10^{-7} to about 7×10^{-6} in ^{60}Fe) over time, consistent with previous results by Vasileiadis et al. (2013).

Enrichment in SLR abundances is also reflected in the spatial distributions of SLRs at different times. The two left panels of Fig. 2 show the distribution of $^{26}\text{Al}/^{27}\text{Al}$ in the cloud for all cells with respect to density and temperature for two different times. The left panel illustrates the distribution just at the end of the quiescent period at $t = 2.2$ Ma, while the middle panel corresponds to the end of the simulation. In both diagrams one can see that the temperature of the gas decreases with increasing density. Also, the spread in $^{26}\text{Al}/^{27}\text{Al}$ is wider for low density gas than for high density gas. Both diagrams reveal that the highest abundances occur for highest temperatures, but due to several recent SNe injections, this property is much more evident at the end of the simulation (middle panel) than after the SN quiet phase (left panel). The significant amount of cells with high temperatures and low density reveals the admixing of enriched gas from SNe explosions into the GMC. To give an overview of the spatial distribution of the SLRs, in particular $^{26}\text{Al}/^{27}\text{Al}$, we present the distribution of $^{26}\text{Al}/^{27}\text{Al}$ inside our entire box with the visualization software VAPOR. The color-scheme represents $^{26}\text{Al}/^{27}\text{Al}$ ratios from a lowest value of about 3.9×10^{-8} to highest values of about 5.6×10^{-2} . For clarity, we set the floor values to 10^{-2} (10^{-8}) and colored all values above (below) this value in white (violet). However, because the high $^{26}\text{Al}/^{27}\text{Al}$ values are typically associated with hot and, hence, very low density gas, the gas enriched in SLR does not contribute significantly to the overall mass distribution in the GMC. The variability in $^{26}\text{Al}/^{27}\text{Al}$ ratios present in dense and cold star-forming gas is much more limited relative to that of the entire GMC.

To quantify the distribution of SLR abundances in our GMC at different times more accurately, we plot the $^{26}\text{Al}/^{27}\text{Al}$ and

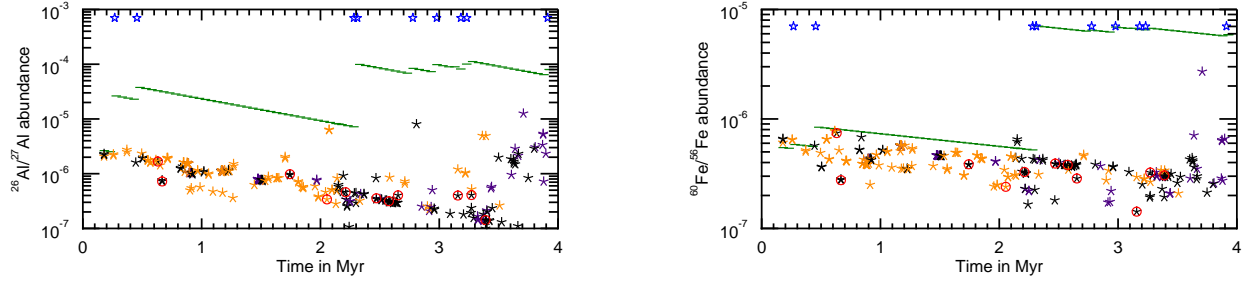


Figure 1. The two panels illustrate the SLR-ratios for all the sinks in the mass range $0.2M_{\odot}$ to $0.5M_{\odot}$ (purple asterisks), $0.5M_{\odot}$ to $2.5M_{\odot}$ (black asterisks), $2.5M_{\odot}$ to $8M_{\odot}$ (orange asterisks) and the average value of all the gas (green horizontal line) vs. time of formation in the RAMSES simulation. The red circles mark the 11 stars that are selected for zoom-ins. The blue stars in the upper part of both plots indicate times of supernovae explosions – they do not reflect the SLR abundance/injection of the supernovae. Left panel: $^{26}\text{Al}/^{27}\text{Al}$; right panel: $^{60}\text{Fe}/^{56}\text{Fe}$

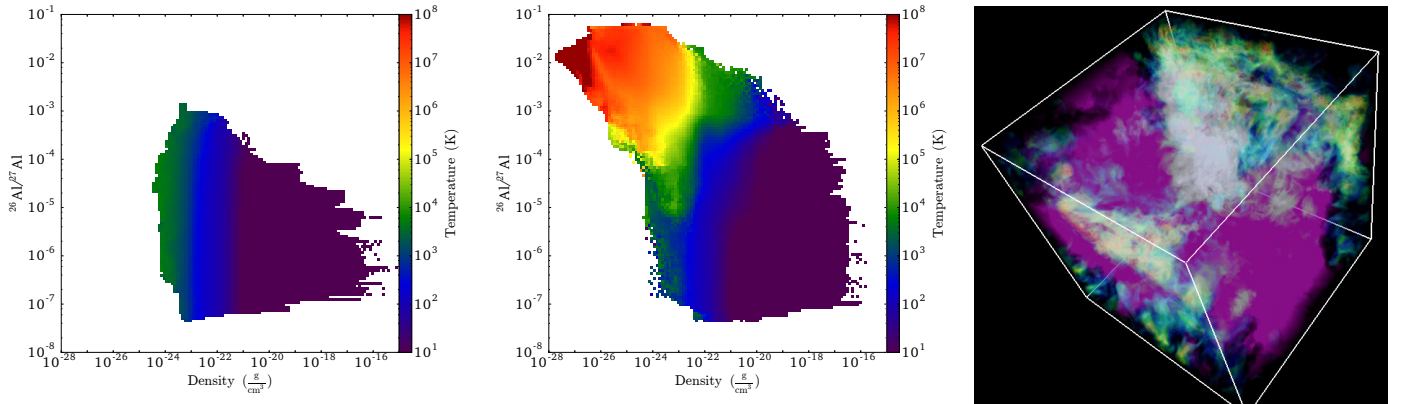


Figure 2. Distribution of $^{26}\text{Al}/^{27}\text{Al}$ abundance inside the entire box of all the cells just at the end of the SN quiet period at $t = 2.2$ Ma (left panel) and at the end of the simulation $t = 3.9$ Ma (middle panel) in dependence of their density. The colors in the diagram represent the temperature gas temperature from cold (purple) to warm (red). The right panel illustrates how $^{26}\text{Al}/^{27}\text{Al}$ is distributed in the GMC at the end of the simulation. White color represents low abundances (10^{-7}), while white represents high abundances (10^{-2}).

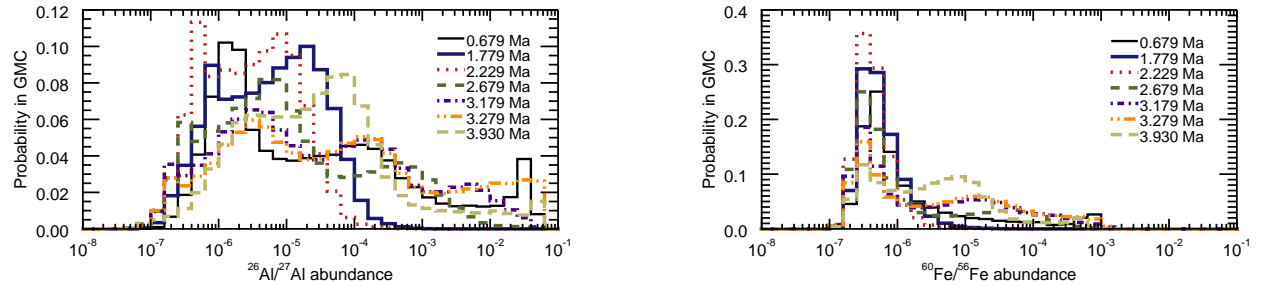


Figure 3. The two panels illustrate the probability distribution of SLR-values in logarithmic steps of 0.1 at times briefly after the formation of star 1 and 2 ($t =$), star 3 ($t =$), star 5, star 6, star 7, star 8 and 9 and at the end of the simulation. Left panel: $^{26}\text{Al}/^{27}\text{Al}$; right panel: $^{60}\text{Fe}/^{56}\text{Fe}$

$^{60}\text{Fe}/^{56}\text{Fe}$ distribution in the form of histograms in Fig. 3. The distributions clearly show that large spatial heterogeneities in $^{26}\text{Al}/^{27}\text{Al}$ abundance exist throughout the entire GMC due to supernovae enrichments. The SLR ratios cover a range of up to 6 orders of magnitude for $^{26}\text{Al}/^{27}\text{Al}$ and up to about 4 orders of magnitude for $^{60}\text{Fe}/^{56}\text{Fe}$ at times not too long after recent SNe events. Furthermore, the distribution is narrower and the GMC lacks very high values of

⁴ We skip illustrating the histogram at the time of formation of star 4 for reasons of readability of the plot. Since the time briefly after star 5 already reflects the end of the long supernova-free phase, the corresponding histogram of star 4 is similar to the one of star 3 and star 5.

SLRs at the end of more quiescent periods (blue solid line, red dotted line). Comparing the histogram for $t = 2.229$ Ma corresponding to the end of a quiescent period with the distribution shortly after the two first supernovae injections at $t = 0.679$ Ma shows that the maximum SLR values are about two orders of magnitude lower as seen in Fig. 2. This significant decrease in ^{26}Al and ^{60}Fe abundance observed at the end of the quiescent period cannot be explained by radioactive decay and, instead, must reflect progressive admixing of the SLR-enriched high density gas with older, lower density gas present in the GMC. Considering the range of abundances found in our model, both the canonical value measured in bulk

CV CAIs as well as lower values measured in FUN CAIs are well represented within the range found in our simulation, although the majority of star forming gas is of lower abundance.

Similarly to Fig. 1, we illustrate in Fig. 4 (left panel) the evolution of the average $^{60}\text{Fe}/^{26}\text{Al}$ ratio in the GMC together with the abundances of the individual stars at their time of formation (asterisks) and the exploding SNe. Although the average ratios varies due to the different decay times of ^{60}Fe and ^{26}Al as well as the different supernovae enrichments during the evolution of the GMC, the value generally decreases from about 0.3 to about 0.16 at the end of the simulation due to the larger amount of SNe that admix more ^{26}Al than ^{60}Fe into the GMC. Again, this value is in agreement with Vasileiadis et al. (2013), who found an average value of about 0.2. Furthermore, the value at later times is also consistent with the galactic value of 0.15 ± 0.06 (Diehl et al. 2006; Wang et al. 2007). Our average value is higher than the galactic value throughout the entire evolution of about 4 Ma, but might eventually become lower if we had continued the simulation for a longer time. We argue that despite of natural fluctuations of the $^{60}\text{Fe}/^{26}\text{Al}$ value, the overall trend of a decrease is expected for the following reason. Considering that supernovae generally admix less Fe relative to Al for decreasing masses of the progenitor, the $^{60}\text{Fe}/^{26}\text{Al}$ will naturally decrease in GMCs over time. This argument is also supported, when looking at the distribution of $^{60}\text{Fe}/^{26}\text{Al}$ ratios inside our cloud Fig. 4 (right panel) at the same times as considered in Fig. 3. Since our GMC has already evolved long enough before the start of our simulation, the less massive supernova occurs already at the beginning of our simulation. Although somewhat counter-intuitive, the associated distribution (black solid line) reveals that the lowest $^{60}\text{Fe}/^{26}\text{Al}$ ratios occur after a low-mass supernova. In general however, the early SLR abundances are predominantly dominated by enrichments of short-lived heavy SNe, while longer-lived low mass SNe mostly occur at later times and cause new injections. At this point, we emphasize the difficulties of measuring and estimating one single $^{60}\text{Fe}/^{26}\text{Al}$ value for a GMC considering the large range of $^{60}\text{Fe}/^{26}\text{Al}$ ratios reflected in Fig. 3 and Fig. 4 (right panel) present throughout the entire GMC. Although mixing occurs inside the GMC, fluctuations are still significant indicating that the process of mixing occurs on longer timescales relative to that depicted in our simulations.

To better understand the heterogeneities inside the GMC, we compare the time scales that are relevant for mixing of the SLRs. The sound crossing time

$$t_{\text{cross}} = \frac{l}{c_s}, \quad (1)$$

where l is a characteristic length and c_s is the sound-speed is the relevant time scale for mixing, while the average time between different supernovae $t_{\Delta\text{SN}}$ provides the time between supernova enrichments. Given that nine supernovae explosions occurred in roughly 4 Ma during our simulation, we set $t_{\Delta\text{SN}}$ to 450 ka. The characteristic length l is the size of the GMC and since the GMC is a periodic cubic box, l varies from at least $l_{\text{min}} = 20$ pc to at most $l_{\text{max}} = \sqrt{3} \times 20^2$ pc ≈ 35 pc. The sound-speed of an ideal gas is given by

$$c_s = \sqrt{\frac{\gamma k_B T}{\mu m}}, \quad (2)$$

where γ is the adiabatic index, k_B is the Boltzmann-constant, T is the temperature, μ is the molecular weight and m is the mass of a single molecule. Given that molecular hydrogen H_2 is responsible for most of the mass in GMCs, we consider $\mu = 2$ and $m = m_H = 1.6733 \times 10^{-24}$ g. Although temperatures can be very different in the GMC, especially in the vicinity of a recent supernovae, we consider typical temperatures of 10 to 50 K for most of the gas in the GMC consistent with observations (Blitz 1993; Solomon & Rivolo 1989). Thus, we adopt a value for the sound-speed in between 200 m s^{-1} and 500 m s^{-1} . Giant Molecular Clouds are supersonic and assuming a Mach number of 10, we obtain typical crossing times of about 5 to 17.5 Ma. This is higher than $t_{\Delta\text{SN}} \approx 450$ ka by more than one order of magnitude, which explains the heterogeneous SLR abundance in the gas of the GMC.

3.2. Abundance of SLRs in stars

After we have shown that SLR abundances of the gas are heterogeneous, we investigate to what extent, the heterogeneity is present in the stars (represented by the asterisks in Fig. 1. Altogether 252 stars of masses higher than $0.2M_\odot$ form in between $t = 0$ and the end of the simulation of which 46 evolve to masses higher than $8 M_\odot$ and will end their lives in SN explosions. As mentioned earlier, none of these stars has exploded in a supernova event by the end of the simulations. The GMC also contains lower mass stars, but we exclude stars of masses lower than $0.2M_\odot$ because the minimum cell size of 126 AU is not sufficient to properly resolve the formation process of the lower mass stars. As we are mostly interested in the evolution of solar mass stars and due to the lack of radiative transfer, we also exclude the high mass stars for our analysis and only focus on the 206 stars in the range of $0.2M_\odot$ to $8M_\odot$. In agreement with Vasileiadis et al. (2013) and Gounelle et al. (2009), the stars show different relative abundances in ^{26}Al (varying from about 1×10^{-7} up to about 1×10^{-5}), as well as in ^{60}Fe (varying from about 1×10^{-7} up to 3×10^{-6}) at their time of formation. Moreover, similar to the distribution of all the gas in the cloud, the initial abundances are on average lower and show a narrower spread in abundance than seen at later times.

However, there are significant differences in the overall distribution of SLR abundances in the gas and the SLR abundances of the stars. The stars show a smaller range of abundances than the gas. It is striking that the stars have abundances that always lie below the average abundance in the gas at that time. Moreover, a significant amount of stars show abundances that follow the decay curve of the average value of the gas at the very beginning of the simulation (the barely visible small green lines). We interpret this result such that these stars form from the gas of this first rather old gas reservoir. By the time of running the parental run, we had not implemented the tracer particle feature. Otherwise, we could have followed the history of the gas from at least one supernovae injection during the evolution of the GMC. Nevertheless, we can use the decay time of the SLRs as a clock to draw some qualitative conclusions about the origin of the gas in stars. In agreement with the delay of enriched SLR abundances for the stars in our box, we suggest that although highly SLR enriched gas from supernovae is present in the GMC, it does not contribute to the formation of stars until at least several 100 ka later. This is in agreement with results from Vasileiadis et al. (2013), who followed the motion of gas injected in SNe by us

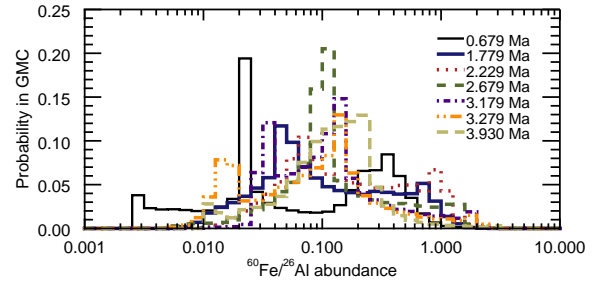
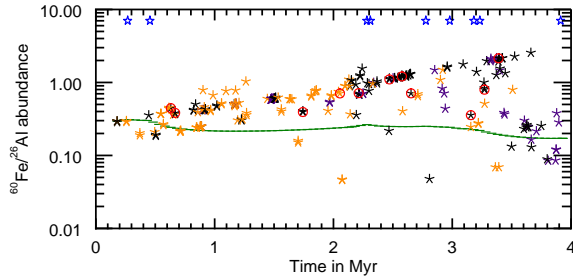


Figure 4. The plot illustrate the evolution of the average $^{60}\text{Fe}/^{26}\text{Al}$ in the gas phase of RAMSES simulation (green horizontal lines) together with the ratios inside the stars (black asterisks). The blue stars in the upper part of both plots only indicate times of supernovae explosions, but no SLR abundance of the supernovae.

ing tracer particles and estimated that it takes of the order of 1 Ma until such gas is incorporated in star forming cores. Observations show that stars form in regions of cold, dense gas. Thus, it is perspicuous that the gas needs time to cool before it can take part in star formation. This is in agreement with the results seen in Fig. 2 (left and middle panel), as well as in Fig. 3. In general, the gas covers a large range of ratios and densities. However, $^{26}\text{Al}/^{27}\text{Al}$ abundances higher than 10^{-3} only occur for densities that are lower than $10^{-13} \text{ g cm}^{-3}$, and can thus not contribute to star formation yet. A thorough view on the plot shows that only a few cells have densities higher than $10^{-16} \text{ g cm}^{-3}$. These cells correspond to potential star forming cores and the gas does not show such large spreads in $^{26}\text{Al}/^{27}\text{Al}$ ratio as for lower densities. Considering that the densities of the star forming cores are several orders of magnitude higher than the SLR-enriched gas in the vicinity of recent SNe indicates the difficulty to contaminate the star forming cores with new gas of different abundance. Given that high abundances must be associated with recent supernovae activities, we conclude that the gas needs time to cool sufficiently before it is able to clump and subsequently to form stars only from the gas with lower SLR ratio.

3.3. SLR distribution in vicinity of stars at early times

With respect to the measured differences in $^{26}\text{Al}/^{27}\text{Al}$ between ordinary CAIs and FUN CAIs of more than one order of magnitude, it is of particular interest to investigate, whether such differences occur during the accretion process. It is generally accepted that the formation of CAIs (both CV and FUN types) is restricted to the very early phase of star formation and very close to the star, probably only to the first few ten thousand years and the inner AU (Krot et al. 2009; Holst et al. 2013). Since the resolution around the stars is 126 AU and the time steps in the parental run already is 50 ka, we cannot resolve the surrounding to this level for all the stars in our simulation. However, late-stage conatmination of an accreting star by freshly synthesized SN material requires that the differences in abundance originate at distances far beyond the sizes of star forming cores. Therefore, we test, whether significant differences in abundance occur within 500 AU of the star 50 ka after its formation. In Fig. 5, we show the number of cells around the stars in the mass range of $0.2M_{\odot}$ to $8M_{\odot}$ that show ten times higher $^{26}\text{Al}/^{27}\text{Al}$ ratios within a distance of 5000 AU and less than 50 ka after the birth of the star with respect to the abundance in the corresponding star. Altogether only nine of the 206 stars that have accreted to $0.2M_{\odot}$ to $8M_{\odot}$ show contaminations within 5000 AU of more than a factor of ten, while only two of these stars are heavier than $1M_{\odot}$. We emphasize that all of the cells with very different abun-

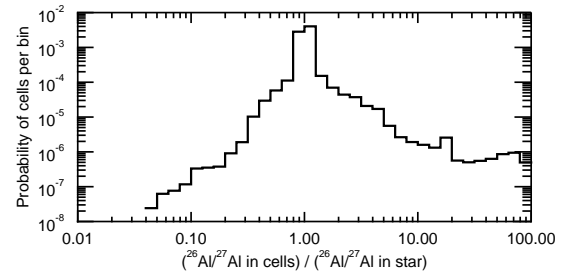


Figure 5. Histogram showing the probability distribution for relative difference in $^{26}\text{Al}/^{27}\text{Al}$ of cells within a radius of 5000 AU compared to their host star.

dance are at least 1500 AU away from the star and belong to times already up to 50 ka after the star has formed. Hence, we do not see any contaminations at early times relevant for CAI formation ($t < 10 \text{ ka}$) that can account for the measured differences of $^{26}\text{Al}/^{27}\text{Al}$ in FUN CAIs and ordinary CAIs.

To ensure that this result is robust, we selected a few stars to follow their formation phase with higher resolution. The eleven stars selected for zoom-in are marked with red circles in Fig. 1. Ten of the eleven stars accreted between 1 and $2M_{\odot}$. Additionally, we also took into account one star that accreted to more than $7M_{\odot}$.

Figure 6 and Fig. 7 show the temporal evolution of the average $^{26}\text{Al}/^{27}\text{Al}$ ratio and $^{60}\text{Fe}/^{56}\text{Fe}$ in spherical shells at distances of 10 AU and 1000 AU as well as their standard deviations for the selected stars. The selected stars have different relative abundances of $^{26}\text{Al}/^{27}\text{Al}$ between 10^{-7} and 2×10^{-6} , while $^{60}\text{Fe}/^{56}\text{Fe}$ ratios are in between 10^{-7} and 8×10^{-7} . Although the stars selected for zoom-ins show abundances below the canonical value of 5×10^{-5} , we emphasize that our selection is valid to test the hypothesis of ^{26}Al enrichment in the solar system through supernova injection. Considering that bulk CV CAIs are supposed to reflect ^{26}Al enrichment after solar birth, the initial abundances in our selected stars are consistent with values less than 3×10^{-6} as measured in FUN CAIs. Since these values are considered to reflect the original abundance in the collapsing pre-solar core, and the fact that higher abundances are available in the GMC, our selection provides an adequate sample to test the injection hypothesis.

As expected from the results obtained by the parental run, the average $^{26}\text{Al}/^{27}\text{Al}$ and $^{60}\text{Fe}/^{56}\text{Fe}$ ratios are almost indistinguishable at different distances from the parent stars (left and right upper panel of Fig. 6 and 7). This suggest a spatially homogeneous distribution of ^{26}Al and ^{60}Fe within 1000 AU

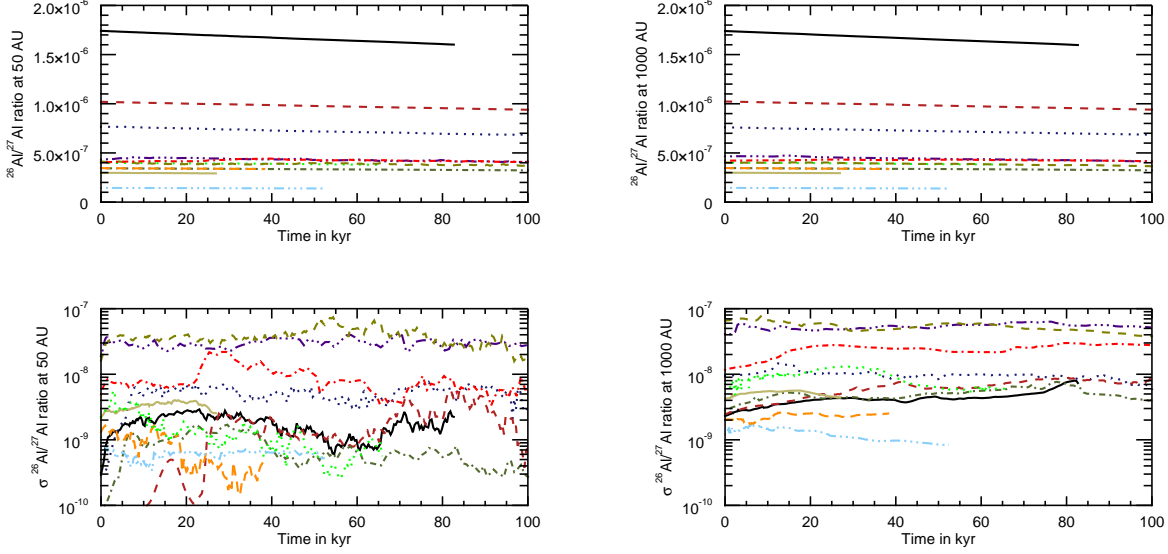


Figure 6. Temporal evolution of the $^{26}\text{Al}/^{27}\text{Al}$ Al ratio (upper panels) and of their standard deviation (lower panels) around the different selected stars in spherical shells at distances of 50 AU (left) and 1000 AU (right) from the corresponding star. Black solid corresponds to star 1, blue dot to star 2, red dash to star 3, dark green dash-dot to star 4, purple dot-dot-dash to star 5, orange dash to star 6, kaki solid to star 7, lime-green dot to star 8, olive green dash to star 9, bright red dash-dot to star 10 and light blue dot-dot-dash to star 11.

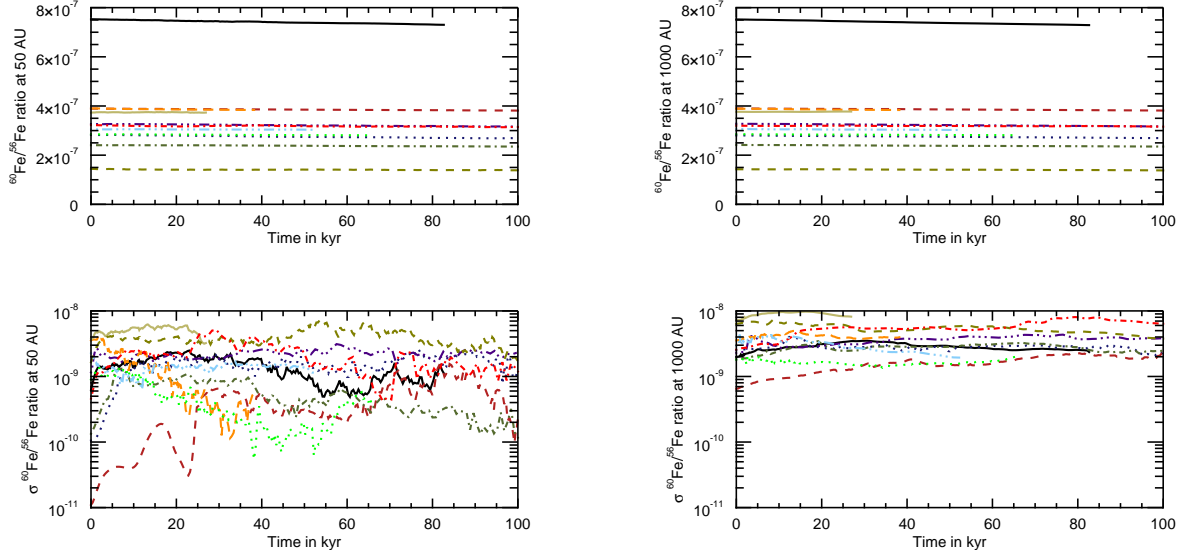


Figure 7. Temporal evolution of the $^{60}\text{Fe}/^{56}\text{Fe}$ ratio (upper panels) and for their standard deviation (lower panels) around the different selected stars in spherical shells at distances of 50 AU (left) and 1000 AU (right) from the corresponding star. Black solid corresponds to star 1, blue dot to star 2, red dash to star 3, dark green dash-dot to star 4, purple dot-dot-dash to star 5, orange dash to star 6, kaki solid to star 7, lime-green dot to star 8, olive green dash to star 9, bright red dash-dot to star 10 and light blue dot-dot-dash to star 11.

during the accretion process for the first 100 Kyr of evolution. We note that the apparent time integrated variability is consistent with the typical decay curve for ^{26}Al and ^{60}Fe . In principle, inflow of gas with different SLR abundances at two different locations and identical in-fall speed could nevertheless cause spatial heterogeneities without affecting the average SLR value, which would be reflected in large deviations from the mean value. However, the ratios deviate only marginally from the average values in the shells as illustrated by plotting the standard deviation from the mean value at distances of 50 AU and 1000 AU in the lower panels of Fig. 6 and Fig. 7. Generally, the different stars all have deviations

that range from less than 1 % to at most 20 % of the mean value. Importantly, the fluctuation observed in the star with the largest fluctuation in $^{26}\text{Al}/^{27}\text{Al}$ ratios (star 9) is still lower by more than one order of magnitude relative to the difference between canonical and FUN CAIs.

To better understand the reason for the spatial homogeneity of ^{26}Al during the accretion, we investigated the origin of the gas and compared it with the SLR distribution at time $t = 0$. The right panels of Figure 8 and Fig. 9 illustrate the $^{26}\text{Al}/^{27}\text{Al}$ distribution of all cells within a distance of 100 kAU around the stars at time $t = 0$ for the eight zoom runs including tracer particles. As indicated by Fig. 6, the gas does not

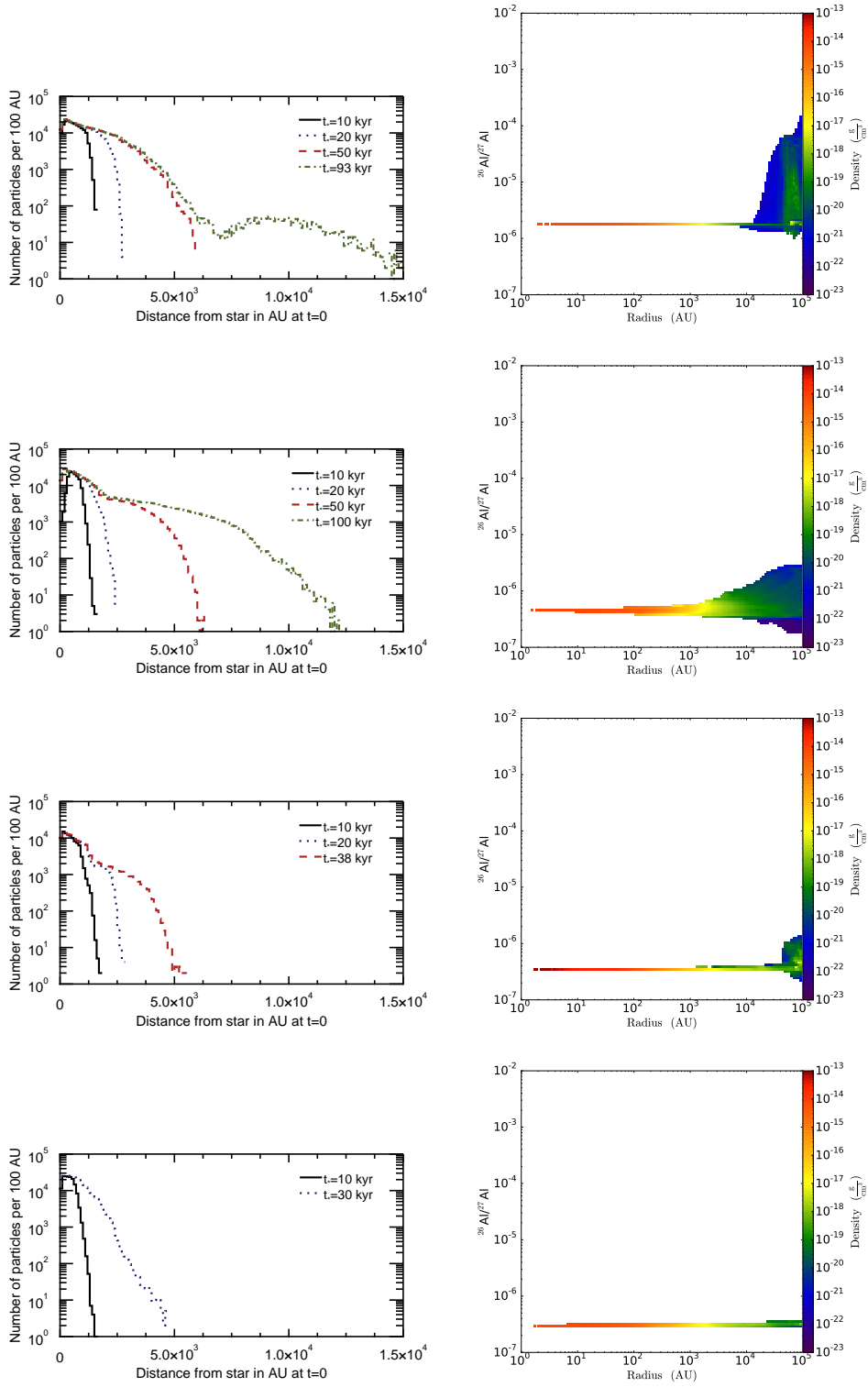


Figure 8. Original location of gas at time of stellar formation that is located within a distance of 100 AU from star 1 (top left), star 5 (second row left), star 6 (third row left), star 7 (fourth row left) at times indicated in the plots. The distances on the x-axis refer to the positions of the gas at the time of star formation. The right panels illustrate the $^{26}\text{Al}/^{27}\text{Al}$ distribution in the gas around the star at the time of its birth.

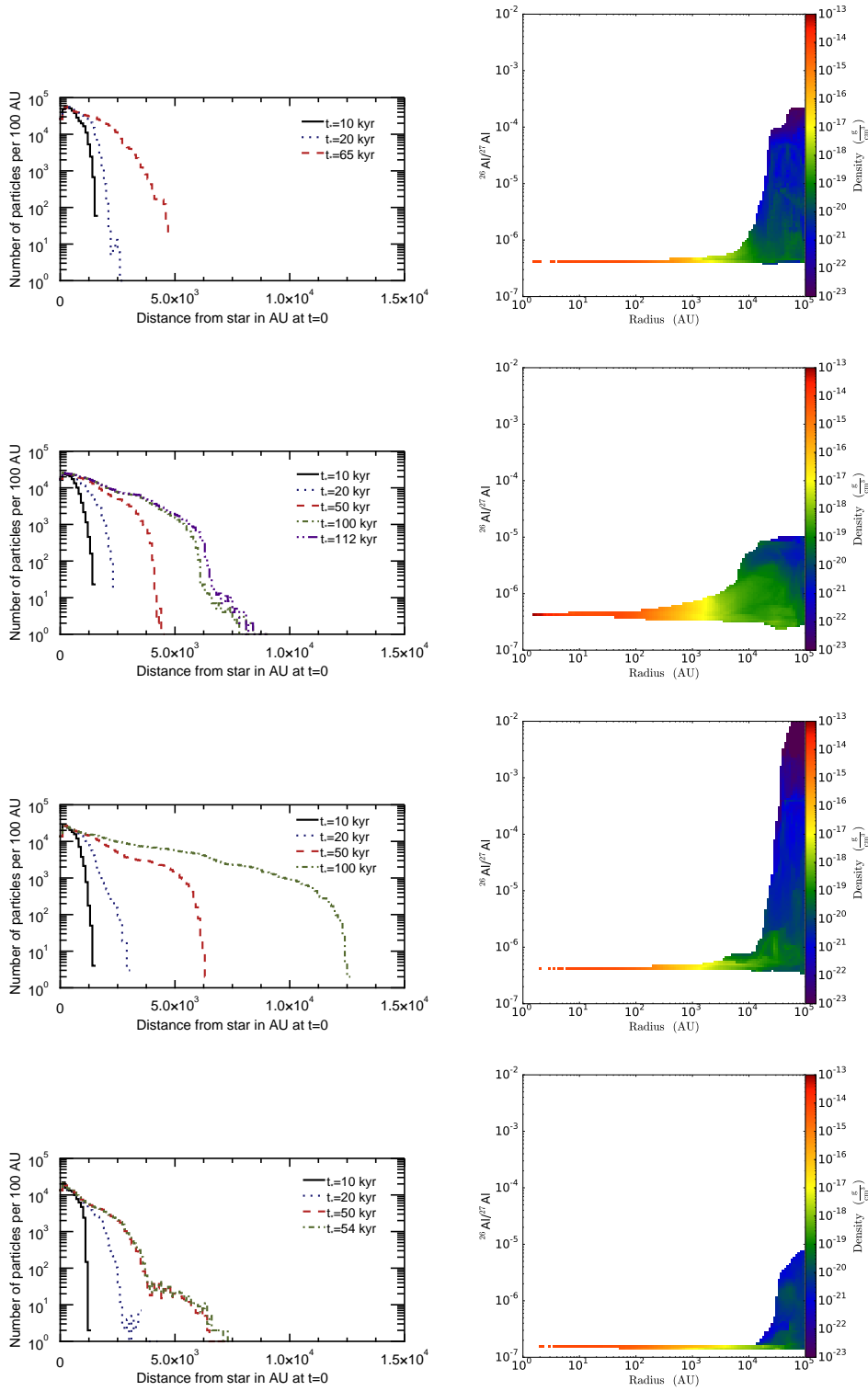


Figure 9. Same as Fig. 8, but for stars 8,9,10 and 11

show spreads of more than a factor of 5 in $^{26}\text{Al}/^{27}\text{Al}$ abundance within about 10 kAU at the time of stellar birth. In contrast, the gas distribution beyond $\sim 10^4$ AU can be of very different abundance, but it is also of much lower density. When following the motion of the gas with tracer particles, we find that – for at least the first 50 ka – all of the gas within the inner 100 AU was located less than 10 kAU away from the star at stellar birth. Considering the narrow spread in SLR abundances for the inner several thousand AU at the time of star formation, this explains why we only see small differences in SLR distribution during the early accretion process of the stars. In Fig. 10, we show the same phase diagrams as in the right panels of Fig. 8 and Fig. 9, but coloring the temperature instead of the density of the gas. Densities decrease with increasing distance from the star and moreover the gas close to the star is of low temperature. This is in agreement with observations that stars form from cores of cold gas of about ~ 10 kAU in size (Enoch et al. 2007).

Our results indicate that heterogeneous accretion processes cannot account for the variability in the $^{26}\text{Al}/^{27}\text{Al}$ ratios between canonical and FUN CAIs during the early stages of star formation, which may appear counterintuitive considering the variability of several orders of magnitude in SRL abundances present within the entire GMC. We consider below the cascade of events leading to star formation in a GMC structure to better understand our results. Turbulent motions inside GMCs pre-dominantly cause the formation of filaments of pc-size inside GMCs. Inside these filaments gas gets further compressed to form pre-stellar cores of sizes of 5 to 10 kAU consistent with theoretical predictions of a Bonnor-Ebert sphere. Eventually, the cores become dense enough to overcome the threshold value for gravitational collapse, and they collapse to stars. Compared to typical sizes of GMCs, sizes of pre-stellar cores are about three orders of magnitude lower and fill only a small part of the GMC (Fig. 2). In order to contaminate a pre-stellar core during formation, it has to be at the boundary of two regions with different SLR-abundances. Nevertheless, we consider the hypothetical case of a pre-stellar core that is located close to such a high difference boundary. Then we are likely to have the following two regimes: On the one hand, densities inside pre-stellar cores are very high compared to the average in the rest of the GMC, on the other hand, SLR enriched gas is associated to recent supernovae events and therefore located in regions of warm gas, and particularly of low density (right panel of Fig. 8 and Fig. 9, Fig. 10). Thus, even if the gas that is in the vicinity of the pre-stellar core is of significantly different abundance, it is difficult to penetrate the core due to the large density contrast.

Although our simulations have not identified the existence of appreciable spatial and/or temporal heterogeneity in SRL abundances during the early accretion phases, we consider the possibility that a pre-stellar core is contaminated by enriched gas at the beginning of its existence when the densities are still rather low. Similarly to our analysis in the previous section for the mixing on GMC scales, we compare the relevant timescales for the icing at the scale of pre-stellar cores, which is the life time of a pre-stellar core with the crossing time of the gas. Observational constraints suggest that the life times of pre-stellar-cores range from 100 ka up to 500 ka (Enoch et al. 2008). As stars form in regions of cold gas of mostly molecular hydrogen, we adopt a value of 10 K for the temperature of the sound-speed as given in 2. Considering radii of pre-stellar cores of about 5 to 10 kAU for a solar-mass star,

we obtain crossing times of about 100 ka to 250 ka, similar to life-times of pre-stellar cores, which could in principle allow for insufficient mixing inside the core. However, our results show only modest variations in SLR ratios and thus we conclude that the cold gas is already well mixed before the formation of the star forming cores. Even if a potential contamination occurs, it only contributes slightly to the abundance per mass and only penetrates the outer edge of the core, from where it takes several ten thousand years for the gas to fall in towards the star (left panel of Fig. 8 and Fig. 9, Fig. 10).

3.4. Late phase: Potential heterogeneity of SLRs at later times

Although we do not detect any differences in $^{26}\text{Al}/^{27}\text{Al}$ at early times, the fact that gas from initial distances beyond 10 kAU accretes to the star over time scales > 100 ka allows for the possibility of contaminations at later times. Therefore, we consider the evolution process of the stellar surroundings, including the protoplanetary disks, at a phase later than the initial ~ 100 ka, which we refer to as the late phase for simplicity. Due to high computational costs, only data for three stars (star 2, 3 and 4) were acquired for the late phase and none of these runs include tracer particles. One of these stars shows enhancements of up to a factor of 2 in $^{26}\text{Al}/^{27}\text{Al}$ within a distance of only 10 AU from the star after about 160 ka (Fig. 11). Such contaminations at later times are possible due to massive accretion of mass onto the young star during the early phase that causes a decrease in density around the star. Hence, it becomes possible for material that was not initially bound to the protostar to approach the vicinity of the star at later times. Unfortunately, we do not have data from simulations including tracer particles for this run to analyze the origin of the gas causing the enrichments. We point out that this late pollution is different from the idea of contaminating the collapsing pre-stellar core or a specific local injection into the protoplanetary disk from a SN (Ouellette et al. 2007). Finally, we emphasize that such contaminations occurring at late stages in our run probably cannot account for differences in ^{26}Al abundance in CAIs considering that temperatures and pressures are too low to form CAIs directly out of the gas phase at this later stage.

4. ORIGIN OF THE VARIABILITY IN THE $^{26}\text{Al}/^{27}\text{Al}$ RATIO BETWEEN CANONICAL AND FUN CAIS

As indicated by the radioactive decay of the SLRs, and the initial average abundance in the gas phase, most of the stars seemed to have formed from the initial gas reservoir present in the GMC. Towards the end of the run more and more stars that potentially would have ended as solar mass stars formed from SLR enriched gas and the spread in SLR abundances seems to be higher among the stars than at the beginning of our simulation (Fig. 1 and left/middle panel of Fig. 2)). In contrast, it appears that the average SLR abundance in the gas reservoir that contributes to star formation is generally enhanced after 3.7 Ma and the spread becomes narrower again. This general enrichment of the reservoir stems from SNe that occurred at the beginning of the simulation in agreement with the increase of the average $^{26}\text{Al}/^{27}\text{Al}$ in the gas phase and Vasileiadis et al. (2013) that the average abundance of $^{26}\text{Al}/^{27}\text{Al}$ for the star forming gas increases for later times in the evolution. Thus, later times of GMC evolution are more favorable for larger variabilities in SLR ratios around stars. Nevertheless, we do not detect any significant contaminations that could account

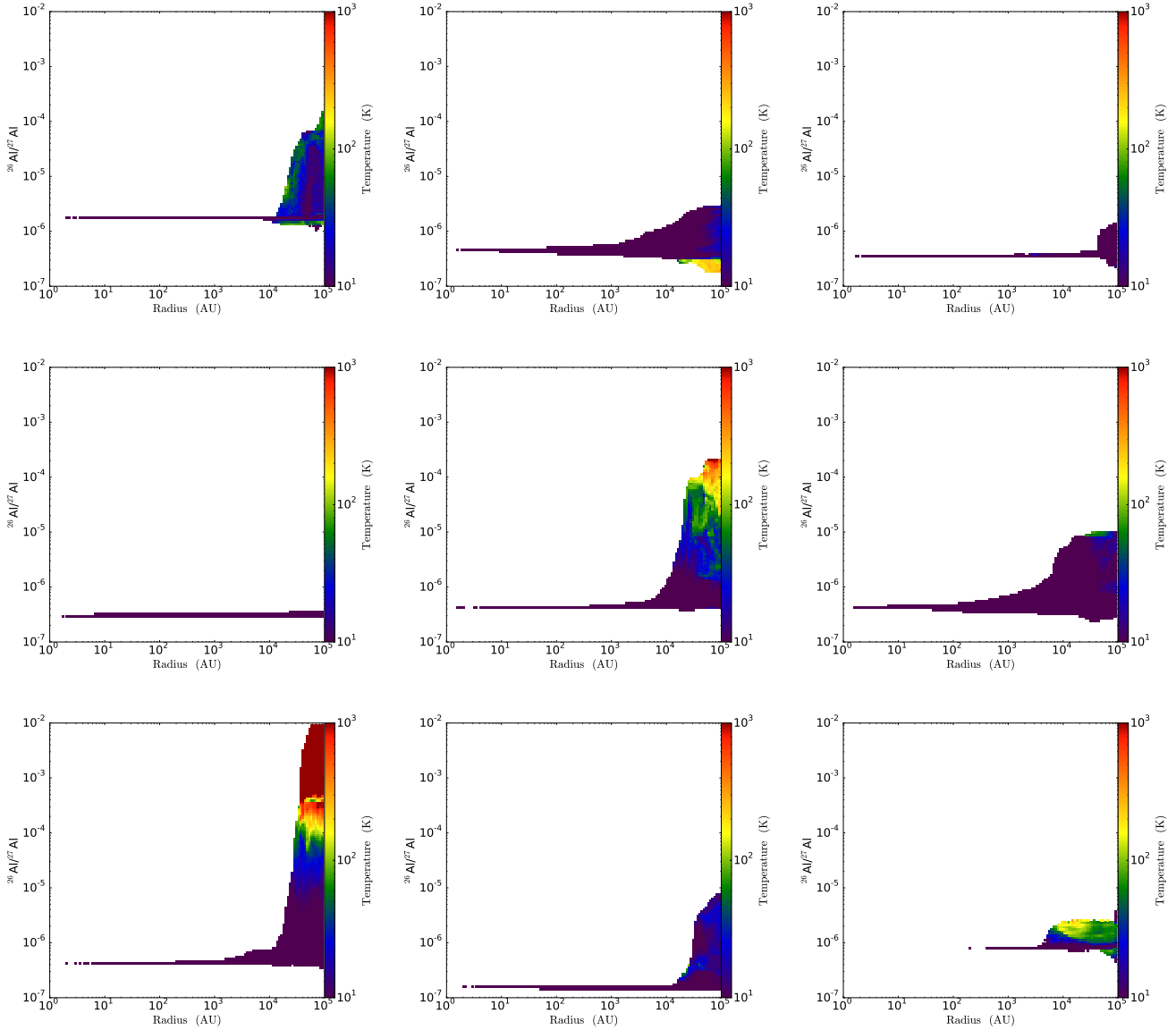


Figure 10. Same as right panel in Fig. 8 and Fig. 9, but showing temperature instead of density from left to right and to bottom for stars 1, 5, 6, 7, 8, 9, 10, 11 and additionally 2. Only cells with $^{26}\text{Al}/^{27}\text{Al}$ ratios below 10^{-2} are illustrated. The lower/upper cut-off value for the temperature is 10/1000 K and values below/above that value are colored purple/red.

for differences in $^{26}\text{Al}/^{27}\text{Al}$ of more than one order of magnitude for any of the more than 200 stars considered in this study. This strongly indicates that the heterogeneities in the solar system measured between canonical and FUN CAIs are of different origin.

4.1. CAIs of extrasolar origin admixed to the disk at later times

In contrast to the early phase, our results suggest the presence of gas with variable $^{26}\text{Al}/^{27}\text{Al}$ ratios in the stellar surrounding during later phases of accretion, namely > 100 ka after star formation. As such, we evaluate the possibility that FUN CAIs represent objects formed around other ^{26}Al -poor solar mass stars located in the vicinity of the proto-Sun and thereafter transported to the Sun via stellar outflows (MacPherson & Boss 2011). Two lines of evidence are in apparent support of such a scenario. First, most stars form in cluster often separated by less than 1000 AU (Lada & Lada

2003). Second, approximately 1 solar mass of material is lost to outflows during the accretion of solar mass type star (Offner et al. 2014). Thus, the cross contamination of nearby nascent systems through stellar outflows appears to be likely the outcome of star formation in clusters. We assess this possibility by investigating the spatial distribution of stars with contrasting $^{26}\text{Al}/^{27}\text{Al}$ values in our simulations. We restrict our analysis to stars more massive than $0.2M_{\odot}$ that formed within a timeframe of 1.6 Myr, as this represent the maximum age different between canonical and FUN CAIs inferred from the ^{182}Hf - ^{182}W system (Holst et al. 2013). In Fig. 13, we show that all pair of stars formed within a distance of 50 kAU have initial $^{26}\text{Al}/^{27}\text{Al}$ values within one order of magnitude, although greater variability is observed at greater distances. Therefore, if correct, our analysis requires the transport of CAI material in the ISM over distance greater to 50 kAU to explain the consorting initial $^{26}\text{Al}/^{27}\text{Al}$ ratios observed

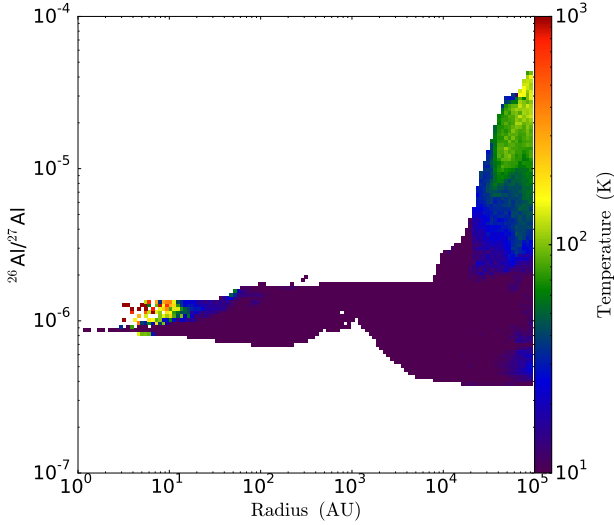


Figure 11. Phase-space diagram for star 2 at $t = 160$ ka after star formation.

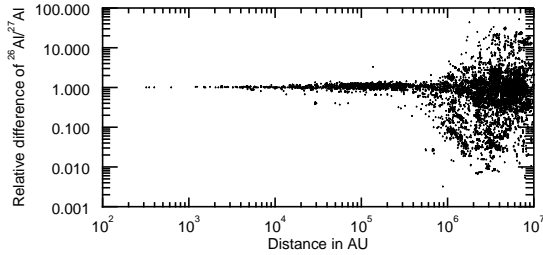


Figure 12. Relative difference in $^{26}\text{Al}/^{27}\text{Al}$ abundance between all stars of mass higher than $0.2M_{\odot}$ and all stars that have an age difference of at most 1.6 Ma with respect to their distance at the time of formation of one of the stars.

between FUN and canonical CAIs, which appears unrealistic.

One might argue that CAIs formed instead around stars lower than $0.2M_{\odot}$ in mass, which are closer to the star. Even with our state of the art zoom-run, we do not resolve the formation of these very low mass stars properly and do not have a reliable statistics for these stars. However, we are confident that the SLR to distance relation would not be very different for low mass stars considering that these stars formed from the same gas reservoir as the higher mass stars. Taking additionally into account the uncertainty that CAIs can travel through the ISM and accrete onto the star-disk system, we expect this scenario as improbable.

4.2. Thermal processing of dust grains

Instead, we argue that measured differences in CAIs and chondrules are most likely induced by physical processes that we neglect. In our model, we only considered the motion of the gas to track the influence from GMC scales down to protoplanetary disk scales. However, observations show that GMCs and protoplanetary disks consist to about 1% of dust. Therefore we suggest thermal processing of solids as a cause of heterogeneities in $^{26}\text{Al}/^{27}\text{Al}$ ratio. A detailed study of thermal processing is beyond the scope of this paper, but we discuss the basics of the process here.

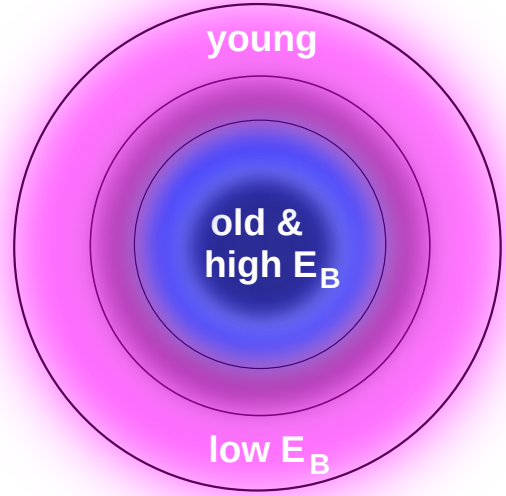


Figure 13. Sketch of a spherical dust grain. Old dust has high binding energy and settles at the center of a grain, while younger dust of lower binding energy is located at the surface layer. Due to radioactive decay older dust components are more likely to contain less ^{26}Al than younger dust grains.

Considering the evaporation time

$$t_{\text{ev}} \propto \nu^{-1} e^{\frac{E_B}{k_B T}} \quad (3)$$

(Boogert et al. 2015; Tielens & Allamandola 1987), where ν is the vibrational frequency, E_B the binding energy of the dust grain, k_B the Boltzmann constant and T the temperature. Approximating dust grains to be perfectly spherical, the energy of one photon $h\nu$, where h is the Planck constant, is assumed to scale with the inverse of the volume of the grains. Thus, we get

$$t_{\text{ev}} \propto a^3 e^{\frac{E_b}{k_B T}}. \quad (4)$$

The dust composition in the ISM consists of grains of different size (up to μm size) and different age. Due to radioactive decay, older dust grains are considered to show lower SLR abundances than younger grains. Taking additionally into account that older grains were exposed to potentially destructive radiation for a longer time, the survived grains have higher binding energies and/or larger grain sizes than the younger grains. Furthermore, older components and thus SLR depleted components are more likely to be in the central layers of the grains, while younger components are more likely to accumulate on the surface of the grains. Thus the younger grain components generally

1. vaporize at lower temperatures,
2. are considered to be in smaller grains and
3. shield the older components from radiation.

In case of star formation, it means that the well mixed dust grains in the pre-stellar core fall in towards the star, where they are exposed to stellar radiation. Since the younger, SLR

enriched components vaporize easier, the gas phase can become locally enriched in SLRs. Depending on the temporally changing strength of irradiation, more or less layers of the dust grains get vaporized, eventually causing a continuous distribution of different $^{26}\text{Al}/^{27}\text{Al}$ ratios in the gas around the star. Due to the short-timescales of this collapsing phase of the order of ka or less, the gas cannot mix to a homogeneous reservoir before CAIs are formed directly out of the gas phase. In this way, CAIs inherit the thermally induced, local heterogeneities of $^{26}\text{Al}/^{27}\text{Al}$ ratios in the early gas phase. Taking additionally into account that chondrules in contrast to CAIs form from solids, this form of thermal processing is also a promising explanation for measured differences in abundances between CAIs and chondrules.

5. CONCLUSIONS

RAMSES and solving the equations for ideal magnetohydrodynamics. For the first time, we followed the dynamics of the gas on small scales relevant for individual star and protoplanetary disk formation and simultaneously account for the large-scale effects induced by magnetic fields and turbulence in the Giant Molecular Cloud. In particular, we analyzed short-lived radionuclide abundances around newly formed stars in simulations of a $(40 \text{ pc})^3$ Giant Molecular Cloud carried out by the AMR code RAMSES. First, we simulated the dynamics in the GMC including injections from SNe with a highest resolution of 126 AU for about 4 Ma. During this time, more than 200 stars with masses in the range of $0.2M_{\odot}$ to $8M_{\odot}$ formed inside the GMC. To model the gas dynamics around in the early phase of star formation in further detail, we particularly investigated the distribution of the $^{26}\text{Al}/^{27}\text{Al}$ ratio during the first ~ 100 ka for eleven of the stars by rerunning their formation process and the early evolution with higher resolution of up to 2 AU. We conclude from our simulations that huge variations in abundance ratios of $^{26}\text{Al}/^{27}\text{Al}$ and $^{60}\text{Fe}/^{56}\text{Fe}$ generated by supernovae explosions exist in Giant Molecular Clouds. However, highly enhanced values only occur in the hot, low density gas located close to recent supernovae events. Over time, the ejecta are cooled down and get incorporated in star-forming gas. Here the gas gets mixed such that the variations in the cold dense gas are modest. None of the more than 200 stars showed variable abundances of a factor of ten or more that can account for the measured difference among canonical CAIs and FUN CAIs. Considering that we also only see marginal variations from the characteristic decay curve of the initial SLR abundance for the gas around the stars selected for zoom-ins, we conclude that the gas in pre-stellar cores is already well mixed before the formation of the stars. We demonstrated that the gas forming the star-disk system accretes from distances within about 10^4 AU, which is in agreement with observations and theoretical predictions for the size of a Bonnor-Ebert sphere for a $1 M_{\odot}$ star. The collapsing gas in the core that forms the star is gravitationally bound and by definition overdense compared to its surrounding. Thus, hot gas from recent supernova injections cannot pollute the stellar environment efficiently in the early phase corresponding to stage 0/I, when the star still has a massive envelope and is strongly accreting from its initial gas reservoir.

However, we point out that the situation changes for times later than about 100 ka, when most of the surrounding gas has accreted onto the star-disk system and the density of the envelope drops by a few orders of magnitude. At these times, gas with different abundance can penetrate the environment

around the star and might potentially lead to high variabilities for the SLR abundance in the protoplanetary disk. As in previous models these variations are related to the production of SLRs by supernovae, but the picture is different in the sense that the SLR enrichments already occur in cold gas. In contrast to a specific injection into the star-disk system, the star moves through the interstellar medium and eventually enters gas reservoirs of different SLR composition. Therefore, the model of supernova injection is also misleading at later times in star formation.

Instead of early heterogeneities SLR distributions in the gas phase around young stars, we suggest that thermal processes of the dust components are the favorable explanation for the enhanced $^{26}\text{Al}/^{27}\text{Al}$ ratios measured in canonical CAIs compared to FUN CAIs. The idea is that older dust grains must have stronger binding energies in order to not be destroyed in the interstellar medium. During the early phase of star formation, temperatures and pressure around the star are very high, but also changing on time-scales of ka or less. Thus, some of the old grains vaporize eventually during the formation process and deplete the SLR abundance locally before that gas shortly later forms CAIs via desorption. Such a mechanism can not only explain the potential large differences in abundances among CAIs, but also the continuous distribution of $^{26}\text{Al}/^{27}\text{Al}$ measured among CAIs.

REFERENCES

- Banerjee, R., & Körtgen, B. 2015, ArXiv e-prints, arXiv:1509.03436
 Bash, F. N., Green, E., & Peters, III, W. L. 1977, *ApJ*, 217, 464
 Blitz, L. 1993, in *Protostars and Planets III*, ed. E. H. Levy & J. I. Lunine, 125–161
 Blitz, L., & Shu, F. H. 1980, *ApJ*, 238, 148
 Boogert, A. C. A., Gerakines, P. A., & Whittet, D. C. B. 2015, *ARAA*, 53, 541
 Bressert, E., Bastian, N., Gutermuth, R., et al. 2010, *MnRAS*, 409, L54
 Connelly, J. N., Bizzarro, M., Krot, A. N., et al. 2012, *Science*, 338, 651
 Diehl, R., Hallöin, H., Kretschmer, K., et al. 2006, *Nature*, 439, 45
 Dobbs, C. L., Krumholz, M. R., Ballesteros-Paredes, J., et al. 2014, *Protostars and Planets VI*, 3
 Ebel, D. S., & Grossman, L. 2000, *Geochim. Cosmochim. Acta*, 64, 339
 Enoch, M. L., Evans, II, N. J., Sargent, A. I., et al. 2008, *ApJ*, 684, 1240
 Enoch, M. L., Glenn, J., Evans, II, N. J., et al. 2007, *ApJ*, 666, 982
 Fahey, A., Zinner, E., & MacPherson, G. 1987, *Meteoritics*, 22, 377
 Franco, J., & Cox, D. P. 1986, *PASP*, 98, 1076
 Fromang, S., Hennebelle, P., & Teyssier, R. 2006, *A&A*, 457, 371
 Fukui, Y., Mizuno, N., Yamaguchi, R., et al. 1999, *PASJ*, 51, 745
 Gnedin, N. Y., & Hollon, N. 2012, *ApJS*, 202, 13
 Gounelle, M., Meibom, A., Hennebelle, P., & Inutsuka, S.-i. 2009, *ApJL*, 694, L1
 Hennebelle, P. 2013, *A&A*, 556, A153
 Holst, J. C., Olsen, M. B., Paton, C., et al. 2013, *Proceedings of the National Academy of Sciences*, 110, 8819
 Jacobsen, B., Yin, Q.-z., Moynier, F., et al. 2008, *Earth and Planetary Science Letters*, 272, 353
 Kawamura, A., Mizuno, Y., Minamidani, T., et al. 2009, *ApJS*, 184, 1
 Krot, A. N., Amelin, Y., Bland, P., et al. 2009, *Geochim. Cosmochim. Acta*, 73, 4963
 Lada, C. J., & Lada, E. A. 2003, *ARAA*, 41, 57
 Larsen, K. K., Trinquier, A., Paton, C., et al. 2011, *ApJL*, 735, L37
 Larson, R. B. 1969, *MnRAS*, 145, 271
 —. 1981, *MnRAS*, 194, 809
 Limongi, M., & Chieffi, A. 2006, *ApJ*, 647, 483
 MacPherson, G. J., & Boss, A. 2011, *Proceedings of the National Academy of Science*, 108, 19152
 MacPherson, G. J., Davis, A. M., & Zinner, E. K. 1995, *Meteoritics*, 30, 365
 Makide, K., Nagashima, K., Krot, A. N., et al. 2011, *ApJL*, 733, L31
 McKeegan, K. D., Chaussidon, M., & Robert, F. 2000, *Science*, 289, 1334
 Miyoshi, T., & Kusano, K. 2005, *Journal of Computational Physics*, 208, 315
 Myers, A. T., Klein, R. I., Krumholz, M. R., & McKee, C. F. 2014, *MnRAS*, 439, 3420
 Nordlund, Å., Haugbølle, T., Küffmeier, M., Padoan, P., & Vasileiadis, A. 2014, in *IAU Symposium*, Vol. 299, *IAU Symposium*, ed. M. Booth, B. C. Matthews, & J. R. Graham, 131–135
 Offner, S. S. R., Clark, P. C., Hennebelle, P., et al. 2014, *Protostars and Planets VI*, 53

- Osterbrock, D. E., & Ferland, G. J. 2006, *Astrophysics of gaseous nebulae and active galactic nuclei*
- Ouellette, N., Desch, S. J., & Hester, J. J. 2007, *ApJ*, 662, 1268
- Padoan, P., Haugbølle, T., & Nordlund, Å. 2012, *ApJL*, 759, L27
—, 2014, *ApJ*, 797, 32
- Padoan, P., & Nordlund, Å. 2002, *ApJ*, 576, 870
—, 2011, *ApJ*, 730, 40
- Padoan, P., Pan, L., Haugboelle, T., & Nordlund, A. 2015, *ArXiv e-prints*, arXiv:1509.04663
- Pan, L., Desch, S. J., Scannapieco, E., & Timmes, F. X. 2012, *ApJ*, 756, 102
- Paton, C., Schiller, M., & Bizzarro, M. 2013, *ApJL*, 763, L40
- Sahijpal, S., & Goswami, J. N. 1998, *ApJL*, 509, L137
- Schaller, G., Schaerer, D., Meynet, G., & Maeder, A. 1992, *A&AS*, 96, 269
- Schiller, M., Connelly, J. N., Glad, A. C., Mikouchi, T., & Bizzarro, M. 2015, *Earth and Planetary Science Letters*, 420, 45
- Shu, F. H. 1977, *ApJ*, 214, 488
- Solomon, P. M., & Rivolo, A. R. 1989, *ApJ*, 339, 919
- Springel, V. 2005, *MnRAS*, 364, 1105
- Teyssier, R. 2002, *A&A*, 385, 337
- Thrane, K., Nagashima, K., Krot, A. N., & Bizzarro, M. 2008, *ApJL*, 680, L141
- Tielens, A. G. G. M., & Allamandola, L. J. 1987, in *NATO ASIC Proc. 210: Physical Processes in Interstellar Clouds*, ed. G. E. Morfill & M. Scholer, 333–376
- Trinquier, A., Elliott, T., Ulfbeck, D., et al. 2009, *Science*, 324, 374
- Truelove, J. K., Klein, R. I., McKee, C. F., et al. 1997, *ApJL*, 489, L179
- Vasileiadis, A., Nordlund, Å., & Bizzarro, M. 2013, *ApJL*, 769, L8
- Wang, W., Harris, M. J., Diehl, R., et al. 2007, *A&A*, 469, 1005
- Wasserburg, G. J., Lee, T., & Papanastassiou, D. A. 1977, *Geophys. Res. Lett.*, 4, 299